Chem

Two $(Ag^{I}_{3}I)_4L_4$ cages elucidate the rules for silver-cluster vertex design

Graphical abstract

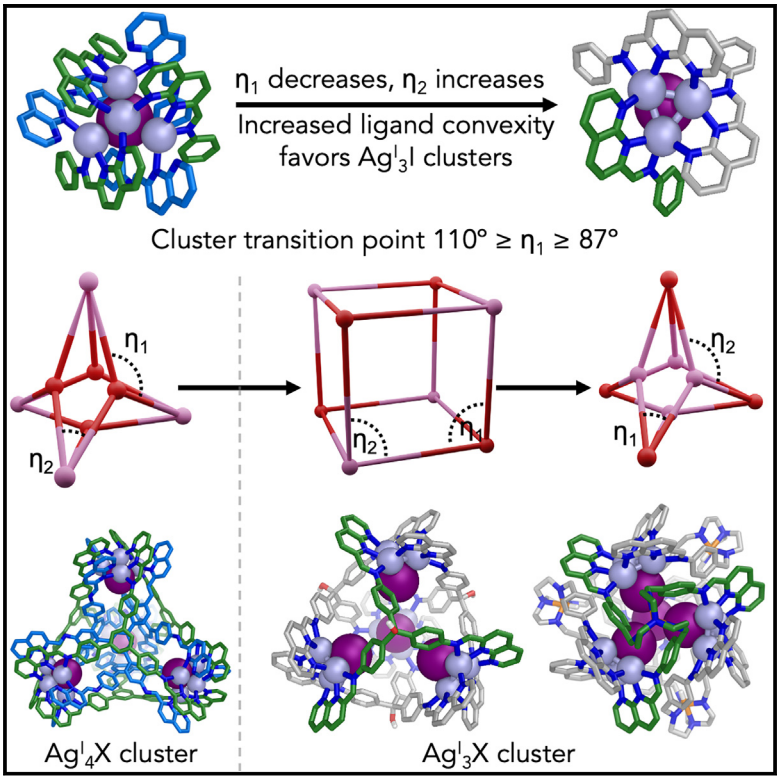

Highlights

- Tetrahedral $Ag^{I}_{12}I_4L_4$ metal-organic cages containing $Ag^{I}_{3}I$ clusters are reported
- Ligand convexity compensates for the large approach angle of the $Ag^{I}_{3}I$ clusters
- The inclusion of ligand convexity advances our understanding of silver clusters
- A taxonomy of silver clusters in metal-organic cages is provided

Authors

Andrew W. Heard, Samuel E. Clark, Charlie T. McTernan, ..., Barbara Rossi, Silvia Marchesan, Jonathan R. Nitschke

Correspondence

smarchesan@units.it (S.M.), jrn34@cam.ac.uk (J.R.N.)

In brief

Atomically defined clusters of silver(I) ions are challenging to synthesize in a predictable and precise manner. Metal-organic cages have proven to be an ideal template to integrate these atomically defined clusters as the vertices of polyhedra. Here, two cages are reported that each contain $Ag^{I}_{3}I$ clusters as vertices, and design rules for governing silver cluster formation in cages are proposed, highlighting the importance of ligand convexity to compensate for the increased approach angle at the cluster vertex.

Heard et al., 2025, Chem *11*, 102456
July 10, 2025
https://doi.org/10.1016/j.chempr.2025.102456

CellPress

Please cite this article in press as: Heard et al., Two $(Ag^{I}_{3}I)_4L_4$ cages elucidate the rules for silver-cluster vertex design, Chem (2025), https://doi.org/10.1016/j.chempr.2025.102456

Chem

CellPress
OPEN ACCESS

Article

Two $(Ag^{I}_{3}I)_4L_4$ cages elucidate the rules for silver-cluster vertex design

Andrew W. Heard,[1,2,7] Samuel E. Clark,[1,7] Charlie T. McTernan,[3,4] Tanya K. Ronson,[1] Petr Rozhin,[5] Barbara Rossi,[6] Silvia Marchesan,[5,*] and Jonathan R. Nitschke[1,8,*]

[1]Yusuf Hamied Department of Chemistry, University of Cambridge, Cambridge CB2 1EW, UK
[2]Astex Pharmaceuticals, 436 Cambridge Science Park, Cambridge CB4 0QA, UK
[3]Francis Crick Institute, 1 Midland Road, London NW1 1AT, UK
[4]Department of Chemistry, King's College London, 7 Trinity Street, London SE1 1DB, UK
[5]Department of Chemical and Pharmaceutical Sciences, University of Trieste, Trieste 34127, Italy
[6]Elettra Sincrotrone Trieste, Basovizza, Trieste 34149, Italy
[7]These authors contributed equally
[8]Lead contact
*Correspondence: smarchesan@units.it (S.M.), jrn34@cam.ac.uk (J.R.N.)
https://doi.org/10.1016/j.chempr.2025.102456

THE BIGGER PICTURE Assemblies containing atomically defined clusters of silver(I) ions have proven useful, but they are challenging to synthesize in a predictable and precise manner.
Metal-organic cages that integrate these clusters as the vertices of polyhedra have been reported. Metal-organic cages have been shown to encapsulate and report on the binding of specific guests, catalyze reactions, and stabilize reactive species. The combination of functions deriving from silver clusters with guest-binding ability could enable new applications if such cages could be made predictably.
In this work, we report two cages that each contain $Ag^{I}_{3}I$ clusters as vertices. We also elaborate on a hypothesis as to the design rules for using silver clusters to build cages.

SUMMARY

Here, we report two $(Ag^{I}_{3}I)_4L_4$ metal-organic cages that each contain a previously unobserved trisilver(I) iodide cluster at their vertices. Clusters containing fewer than 10 Ag^{I} ions are challenging to synthesize in an atomically precise manner. Previous work has demonstrated the potential of the approach of generating such clusters during the formation of higher-order metal-organic cage superstructures, but too few examples were known for design principles to be deciphered. Through analysis of the set of such cages reported herein and previously, we elaborate a set of design principles for their synthesis.

INTRODUCTION

Metal-organic cages[1–6] with metal-cluster or polymetallic vertices[1,2,7–12] have found applications in catalysis,[13–17] selective gas adsorption,[18] and sensing[19,20] and have displayed ferromagnetic properties.[21–23] Many of these polymetallic vertices contain carboxylate bridging motifs[24–26] across early transition metals.[8,9,18,27]

Atomically precise silver clusters comprise a discrete number of silver atoms (from three to hundreds) bound together with the help of argentophilic interactions,[28] where the Ag···Ag distances are smaller than the sum of their van der Waals radii ($\leq$3.44 Å).[29–34] These silver clusters[35–37] possess useful photophysical[38–41] and catalytic properties[42]; however, synthetic strategies often produce a dispersion of species with similar structures and nuclearities.[43–48] Metal-organic superstructures provide useful scaffolds to template the assembly of monodisperse silver clusters with well-defined geometry.[31,49–53] Building on reports of (1,8-naphthyridyl)$_2Ag^{I}_2$[54,55] and carboxylate-bridged (1,8-naphthyridyl)$_2Ag^{I}_2$ complexes,[56] we have synthesized trigonal prisms and octahedra with Ag^{I}_2 vertices,[57,58] double-walled tetrahedra with Ag^{I}_4X cluster vertices (X = Cl, Br, I),[59] and six-stranded helicates with Ag^{I}_4Br, Ag^{I}_4I, and $Ag^{I}_6(SO_4)_2$ termini.[60]

Here, we report two tetrahedral metal-organic cages, where convex ligands containing 1,8-naphthyridyl donors stabilize Ag^{I}_3I cluster vertices through a combination of N–Ag coordination bonds, argentophilic interactions, and silver(I)-iodide ionic bonds. The relationships between ligand approach angle at the vertex and ligand convexity help to explain the emergence of the Ag^{I}_3I cluster type observed in this work. Employing new metal cluster types may help to design new architectures to address more ambitious challenges,[61–64] where greater structural diversity is required.

Please cite this article in press as: Heard et al., Two $(Ag^{I}_{3}I)_4L_4$ cages elucidate the rules for silver-cluster vertex design, Chem (2025), https://doi.org/10.1016/j.chempr.2025.102456

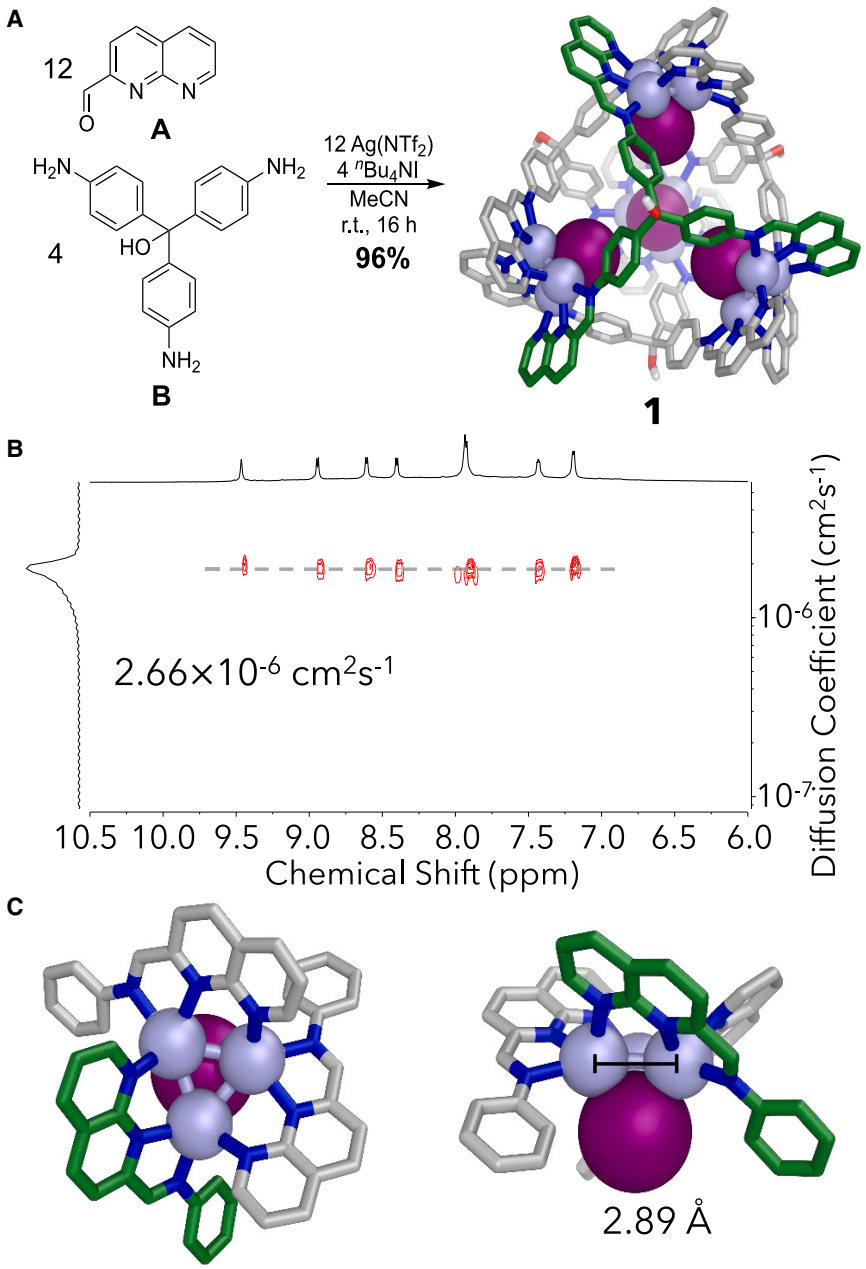

Figure 1. Synthesis and structural characterization of cage 1

(A) Preparation of cage **1** and its X-ray crystal structure, hydrogen atoms, anions, and solvent molecules are omitted for clarity.

(B) DOSY NMR spectrum of **1**, showing a single species with a diffusion coefficient corresponding to a solvodynamic radius of 13.0 Å.

(C) Two views of the $Ag^{I}_{3}I^{2+}$ cluster forming the vertices of **1**, taken from the crystal structure.

The two $(Ag^{I}_{3}I)_4L_4$ cages reported herein incorporate an equilateral triangular $Ag^{I}_{3}I$ cluster, adding to the diversity of cage vertices observed so far. The discovery of this vertex class enables us to offer a preliminary taxonomy of silver-cluster cages, which may offer some predictive power for the preparation of new cages that contain vertices with a predefined number of silver(I) ions.

RESULTS

All of our silver-cluster structures reported to date contain ligands in which some imine nitrogens are not bound to silver(I), contradicting the principle of maximum site occupancy. This principle favors the formation of structures in which all metal ions are coordinatively saturated, and all ligand donor atoms are bound to metal ions.[65]

In this work, 2-formyl-1,8-naphthyridine **A** (Figure 1A) reacted with tritopic pararosaniline **B**, silver(I) bis(trifluoromethanesulfonyl)imide ($^{-}NTf_2$, triflimide), and tetra-*n*-butylammonium iodide (TBAI) to produce $[(Ag^{I}_{3}I)_4L_4](NTf_2)_8$ **1** in 96% isolated yield. The ^{1}H NMR diffusion-ordered spectrum (DOSY) of **1** showed peaks corresponding to a species with a solvodynamic radius of 13.0 Å (Figure 1B; Section S2).

Single-crystal X-ray diffraction using synchrotron radiation at Diamond Light Source revealed the structure of **1** to be a $[(Ag^{I}_{3}I)_4L_4](NTf_2)_8$ metal-organic tetrahedron (Figure 1A; Section S3) with tritopic naphthyridine-imine ligands covering its faces. The vertices of **1** consist of $Ag^{I}_{3}I$ clusters (Figure 1C), a silver-cluster geometry that has not previously been observed to the best of our knowledge. The vertices are separated by 11.6 Å, measured between the centers of each triad of Ag atoms, consistent with the solvodynamic radius observed by DOSY NMR. The equally spaced Ag^{I} ions are 2.89 Å apart. Three naphthyridine-imine ligands are brought together at each vertex, with each naphthyridine bridging two silver ions. Each imine chelates a silver ion together with the closest naphthyridine nitrogen atom.

The synthetic procedure for **1** was repeated with fluoride, chloride, and bromide in place of iodide, and also with no halide template. Although partial imine condensation was observed, ^{1}H NMR signals were broad, suggesting that no well-defined species were formed. This conclusion was supported by DOSY NMR, which showed the absence of any large well-defined species in solution (Section S4).

The mass spectrum of cage **1** was dominated by fragmentation, even under mild ionization conditions (Figures S9–S11); however, the 2+ and 3+ isotope patterns could be seen at low intensities

Please cite this article in press as: Heard et al., Two ($Ag^{I}_{3}I$)$_4$L$_4$ cages elucidate the rules for silver-cluster vertex design, Chem (2025), https://doi.org/10.1016/j.chempr.2025.102456

CellPress
OPEN ACCESS

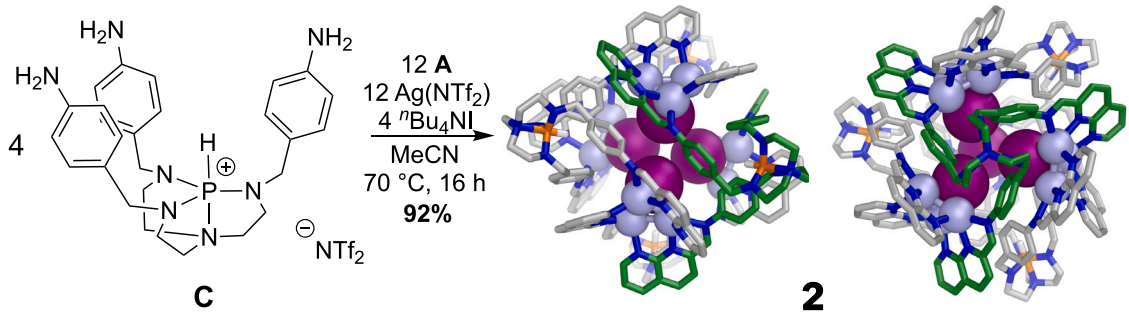

Figure 2. Synthesis of cage 2: Directly, and via a precursor complex

Preparation of cage **2**, shown as the X-ray crystal structure, from subcomponents A and C with TBAI and $AgNTf_2$. Views of the structure are shown down C_2 (left) and C_3 (right) axes. Hydrogen atoms, anions, and solvent molecules are omitted for clarity.

(Figures S12 and S13). The high degree of fragmentation of cage **1** could be due to the fragility of the $Ag^{I}_{3}I$ cluster. The $Ag^{I}_{3}I$ cluster may favor fragmentation to a greater degree than for higher-nuclearity clusters,[59] which require more cooperative binding interactions to be broken during fragmentation.

Cage **2** was prepared through the reaction of cationic triamine **C**, formylnaphthyridine **A**, $Ag(NTf_2)$ and TBAI (Figure 2). DOSY NMR results (Figure S28) indicated a product having a solvodynamic radius of 18.4 Å. Mass spectra were again dominated by fragmentation (Figures S29 and S30), but signals were observed for the 3+ charge state, corresponding to a product with the expected $[(Ag_3I)_4L_4](NTf_2)_{12}$ composition (Figure S30).

Single crystals of cage **2** were grown by vapor diffusion of either benzene or diisopropyl ether into an acetonitrile solution of cage **2** with hexafluorophosphate or tetrafluoroborate counterions, respectively. X-ray data confirmed the formation of tetrahedral **2** (Section S6), containing an $Ag^{I}_{3}I$ cluster isomorphous to the one found in **1**. The ligand centers, measured from the central nitrogen atoms in the **C** residues within **2**, are separated by 17.6 Å, consistent with the solvodynamic radius obtained via DOSY NMR.

The synthesis of **2** was repeated with tetra-*n*-butylammonium fluoride, chloride, bromide, and no added halide in place of the iodide, and the results analyzed by ^{1}H and DOSY NMR (Sections S7 and S8). Although these products showed similar diffusion coefficients to **2** by DOSY, their ^{1}H NMR peaks were broader, and shifted from those observed in iodide-templated **2**. The observations of single DOSY diffusion peaks suggested that comparably sized species to **2** formed in the absence of iodide. Raman spectroscopy provided evidence in all cases for the complete consumption of the aldehyde subcomponent **A**, and the presence of new species with analogous Raman signatures to cage **2**, as discussed below.

Attempts to crystallize the different species formed in the absence of iodide were unsuccessful, following over 800 attempts. Mass spectrometry also showed only putative cage fragments, with no peaks with a greater than 2+ charge observed (Figure S34). These results suggested that products similar to **2** were formed in the absence of iodide, but that these species were less stable. Taken alongside the observation that no isolable analogs of **1** were formed in the absence of iodide, we infer that the softer, more polarizable iodide ion forms stronger Ag···I interactions stabilizing the $Ag^{I}_{3}I$ cluster vertices of cages **1** and **2**, making cages robust enough to isolate and characterize fully. Cage **2** displayed evidence of decomposition in the ^{1}H NMR spectrum at 323 K (Figure S40), further signaling the fragility of the new $Ag^{I}_{3}I$ cluster vertex.

Raman spectroscopy was used to probe cage structure in the solid state and in solution. This technique allows the identification of overtones[59] associated with d^{10}-d^{10} argentophilic interactions.[28] Visible Raman spectra were acquired from dried thin films of cages **1** and **2** dissolved in acetonitrile, as well as the solid cages in powder form. In both cases, peaks associated with metal coordination to the ligands within cages were found in the region 1,550–1,650 cm^{-1} (Figures 3A and 3B) when iodide was used as template.[59] Based on the crystallographic Ag···Ag distances in the vertices of **1**, an empirical Herschbach-Laurie relationship[66–69] predicts a silver-silver stretch frequency of 92 cm^{-1} (supplemental information, Section S9). Although this frequency was not directly observable in solid-state Raman due to broad Rayleigh scattering in the low-frequency region of the spectra, we observed peaks for cage **1** at 317 and 408 cm^{-1} (Figure 3A) that are consistent with combinations or overtones modes of a fundamental band at 91 cm^{-1}, in excellent agreement with the solid-state structure. These signals are redshifted by 3 cm^{-1} relative to those described by Bosnick for ligand-free Ag_3, and, together with an additional band at 538 cm^{-1}, they are ascribed to the Raman signature of the Ag trimer.[69] No signals were detected corresponding to the free subcomponents **A** (aldehyde, 1,703 cm^{-1} attributable to the C=O stretching) and **B** (aniline, 1,611 cm^{-1}), confirming cage integrity and lack of hydrolysis (Figure 3A).

Analogous investigations were undertaken for cage **2**, alongside its congeners formed using F^-, Cl^-, Br^-, and no halide (Figure 3B), as discussed above. The crystallographic Ag···Ag distance of 2.89 Å for **2** corresponds to a silver-silver stretch of 94 cm^{-1}. This distance is consistent with the observation of Raman bands at 313 and 407 cm^{-1} in the spectrum of the bromide analog of **2** (brown trace in Figure 3B). Similar overtones or combination bands were found in the spectra of cage **2** with iodide or without a halide template, albeit at a frequency of 97 cm^{-1}. Signals in the same range for samples obtained with chloride and fluoride were too broad for accurate frequency assignment, suggestive of the presence of greater disorder relative to the crystalline state. Nevertheless, in all cases with or

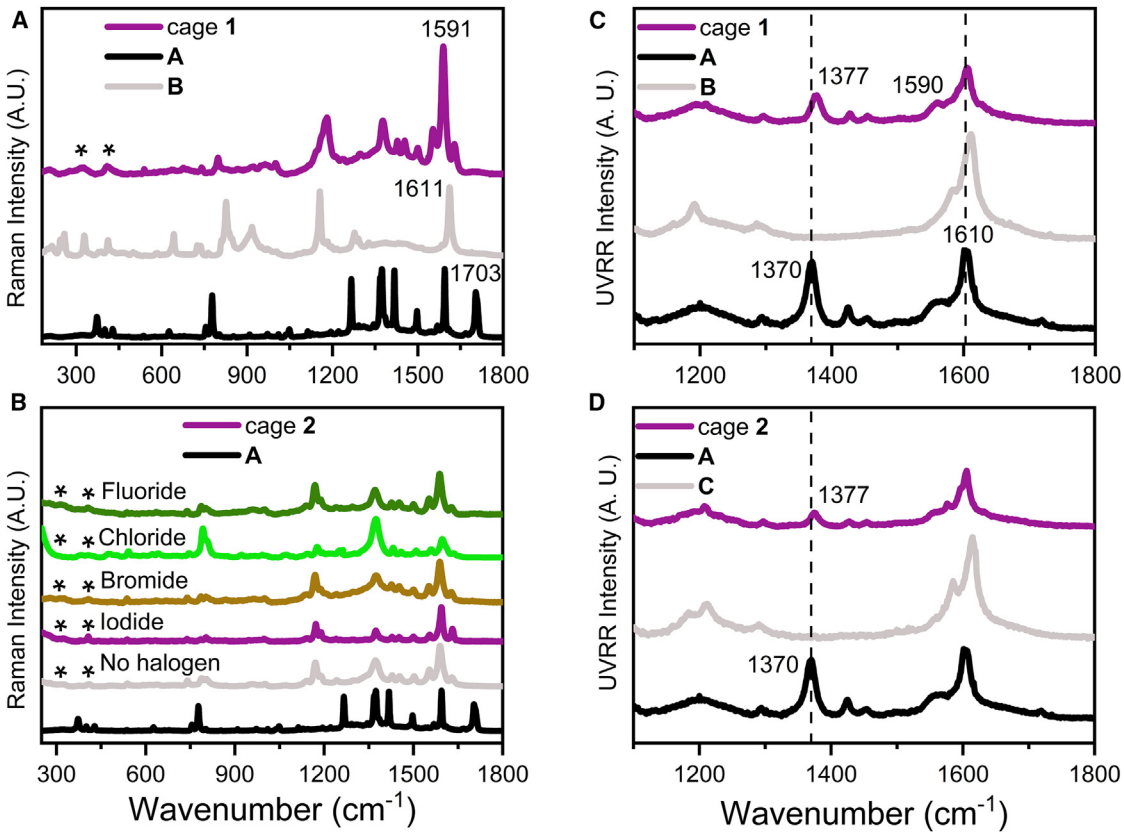

Figure 3. Raman spectra for cages 1 and 2

Visible Raman spectra (A) for cage **1** with iodide as template, and its subcomponents A and B, and (B) for cage **2** and its congeners with different halide templates, as well as its aldehyde subcomponent. UV resonance Raman spectra for (C) cage **1** and (D) cage **2**, together with their subcomponents.

without a halide template, the typical cage signals in the range 1,550–1,650 cm^{-1} and the absence of the aldehyde peak at 1,703 cm^{-1} (black trace in Figure 3B; Section S9) were indicative of the presence of a cage framework.

UV resonance Raman (UVRR) was then employed to directly analyze cages **1** and **2** dissolved in acetonitrile, taking advantage of the higher detection limit associated with the use of an excitation wavelength in the deep UV range. As expected, the UVRR spectra of cage **1** and its subcomponents (Figure 3C) are dominated by Raman signals attributable to their aromatic moieties, whose electronic transitions are close to resonance with the excitation wavelength. The spectrum of cage **1** resembles that of subcomponent **A** with a blue-shift of the intense signals around 1,370 and 1,610 cm^{-1}. The presence of a shoulder at about 1,590 cm^{-1} marks the appearance of a new spectral component for cage **1**, which we infer to derive from the presence of non-covalent interactions. Similar spectra were observed for cage **2** and its subcomponents (Figure 3D).

Both **1** and **2** were screened for their guest-binding abilities (Sections S10 and S11). MoloVol[70] gave an interior volume of 100 $Å^3$ for **1**; however, no significant volume was found in the compact interior of **2**. We inferred that **2** might nonetheless be able to bind guests; a $Fe^{II}_4L_4$ cage incorporating azaphosphatrane-centered subcomponent **C** demonstrated the ability to flex in order to bind guests, with volumes from 35–219 $Å^3$.[71] A set of prospective guests for **2** was thus selected to include inorganic anions and aromatic and aliphatic compounds.

Changes in the ^{1}H NMR spectrum of cage **1** were observed following the addition of small organic guests (toluene, *cis*-decalin) or small anions (ReO_4^- and ClO_4^-). Although the mode of binding for anionic guests could not be definitively assigned, analysis of X-ray data gathered from a sample of **1** containing toluene showed toluene at the edges of the cage in a 1:6 binding stoichiometry (Section S10).

Anionic guests (ClO_4^-, ReO_4^-, BF_4^-, and PF_6^-) were observed to bind to cage **2**; however, no binding was observed for aromatic guests (Section S11). X-ray structures of the BF_4^- and PF_6^- salts of **2**, and shifts in ^{1}H NMR peaks, suggested that this binding occurred within a binding pocket formed between ligands close to the cationic vertices, leading to both electrostatic and dispersion as driving forces for binding. Despite the flexibility of **C**,[71] we thus infer that the closed form of **2** observed in the crystal may persist in solution.

DISCUSSION

The $Ag^{I}_{3}I$ clusters that form the vertices of **1** and **2** constitute the fourth distinct silver cluster structure type synthesized through

the subcomponent self-assembly of formylnaphthyridine **A** and multitopic amine ligands around silver(I). Comparison of these clusters and the superstructures that they form allows for the construction of a preliminary taxonomy, which may be of use to guide the synthesis of targeted structure types containing different vertices (Figure 5B).

Five structural motifs were found in the Cambridge Structural Database[73] that incorporate multiple silver(I) ions and 1,8-naphthyridine ligands (Table S6). The most frequently observed of these is an Ag^{I}_{2} dimer, formed in eight of the twelve structures. This motif formed the vertices of a trigonal prismatic cage,[57] appearing to correlate with the presence of weakly coordinating anions such as perchlorate,[54] hexafluorophosphate,[74] and trifluoromethanesulfonate.[55] More strongly coordinating polyatomic anions that are capable of bridging metal cations are observed to template larger clusters, with carboxylates forming $Ag^{I}_{4}(O_2CR)_2$ rhombic clusters[56] and sulfates generating $Ag^{I}_{6}(SO_4)_2$ clusters.[60]

The relationship between two angles helps elucidate the formation of the $Ag^{I}_{3}I$ cluster vertices of cages **1** and **2**. Variation of the approach angle (θ)[75] between the chelate plane of the ligand and the principal C_3 symmetry axis of the cluster (Figure 4A) provides insight as to the formation of previously reported $Ag^{I}_{4}X$ clusters[59,60] versus the new $Ag^{I}_{3}I$ cluster vertex. The bridging role of naphthyridine in the $Ag^{I}_{3}I$ clusters is only possible for larger approach angles ($\theta_{cage\ 1}$ = 52°, $\theta_{cage\ 2}$ = 56°, Figure 4A), which are greater than those observed in the case of a six-stranded helicate[60] (16°) or the inner (34°) and outer (33°) ligands of a double-walled tetrahedron[59] (right, Figure 4A).

The convexity of the ligands assembled from subcomponents **B** and **C** compensates for the increase in θ for the $Ag^{I}_{3}I$ cluster vertices (Figure 4B). The ligand convexity is defined as the apex angle ϕ of a cone, with a base consisting of the plane defined by the three aniline-derived imine nitrogen atoms and the cone apex at the closest junction point of the three ligand arms (Figure 4B). The ligand of cage **1** has a cone angle of $\phi_{cage\ 1}$ = 135°, and the ligand of cage **2** is more convex, with $\phi_{cage\ 2}$ = 64°. Compared with our previously published double-walled tetrahedron, containing a rigid, flat ligand (ϕ_{DWT} = 171°),[59] we infer that the increased ligand convexity of **1** and **2** stabilizes this new $Ag^{I}_{3}I$ cluster vertex type, with its larger approach angle θ.

The angle compensation is similar to mathematical descriptions of heterocubes published by O'Keeffe and Yaghi,[72] which also apply here (Section S12). Measuring the angles between the center of the ligand (η_1, red sphere Figure 5A) and the center of the cluster (η_2, pink sphere Figure 5A) provides further insight into how the convexity of the ligand affects the approach angle, governing the cross-over point from an $Ag^{I}_{4}I$ cluster to an $Ag^{I}_{3}I$ cluster. Using the heterocube rules explaining the relationship between η_1 and η_1,[72] we can characterize the double-walled tetrahedron (η_1 = 110°, η_2 = 65°) as close to an ideal tetrahedron. Decreasing η_1 and increasing η_2 to 90°, in the case of a face-capped tetrahedron, approaches the geometry of an ideal heterocube. Cage **1** lies just beyond this limit, with η_1 = 87° and η_2 = 93°. A more convex ligand further decreases η_1 and increases η_2, as in cage **2** (η_1 = 52°, η_2 = 117°), favoring the $Ag^{I}_{3}I$ cluster.

The crossover point from an $Ag^{I}_{4}I$ cluster with a smaller approach angle (Figure 5A, left) to an $Ag^{I}_{3}I$ cluster with a larger approach angle (Figure 5A, right) lies between 110° $\geq \eta_1 \geq$ 87°, with ligand convexity key to this cluster transition. Cages **1** and **2** both lie on the same side of this transition, with $\eta_1 \leq$ 87°. Ligands with greater convexity can compensate for the associated increase in approach angle by integrating the new $Ag^{I}_{3}I$ vertex cluster reported in this work.

From these parameters and the observations noted above, we outline a preliminary taxonomy of the known silver-naphthyridine architectures in the form of a flow chart (Figure 5B). When iodide is present, the use of a ligand with greater convexity and a shallower approach angle, as in **1** and **2**, is observed to favor the formation of the $Ag^{I}_{3}I$ cluster (Figure 5B). These parameters allow the naphthyridine moieties on each ligand to bridge Ag_2 pairs in the cluster plane. In contrast, planar ligands require a smaller approach angle, precluding naphthyridine from performing the same bridging role. The presence of the apical silver atom in the $Ag^{I}_{4}I$ cluster allows the ligand in these cases to bind via both naphthyridine nitrogen donors. In the previously reported $(Ag^{I}_{4}I)_2L_6$ six-stranded helicate,[60] the limited flexibility of the 2,2′-dimethylbenzidine ligand core again favors the $Ag^{I}_{4}I$ cluster structure.

Conclusions

In summary, we present two cage scaffolds capable of stabilizing a new $Ag^{I}_{3}I$ vertex type. The fragility of these $Ag^{I}_{3}I$ cluster-cages was reflected in their high temperature NMR spectra and significant MS fragmentation. This work thus builds upon and extends prior studies involving cluster vertices that incorporate early transition metals[8,9,18,27] and bridging carboxyl ligands.[24–26] The vertex type reported in this work shows how tuning ligand convexity and ligand approach angle can allow access to new silver clusters.

The taxonomy of vertices presented in Figure 5B may thus serve to elucidate design rules for the integration of silver clusters into the vertices of cages prepared through subcomponent self-assembly using formylnaphthyridine **A**. In the absence of a coordinating anionic template, such as iodide, sulfate, or a carboxylate, disilver vertices might be expected to form. When iodide is present, more convex ligands are anticipated to generate the $Ag^{I}_{3}I$ vertex structure expressed by cages **1** and **2** herein, whereas flat and rigid ligands should instead favor $Ag^{I}_{4}I$ vertices. Such ligands might also generate $Ag^{I}_{6}(SO_4)_2$ vertices with sulfate, whereas carboxylates may bridge pairs of silver(I) ions to generate $Ag^{I}_{4}(O_2CR)_2$ rhombuses.

Following and extending the principles of ligand design described here may enable the preparation of cages with further new cluster vertices. In particular, the ability to generate vertices that incorporate larger approach angles than is currently possible with single metals may enable the preparation of larger polyhedral cage structures, beyond dodecahedra,[76] where the sum of angles around trigonal vertices approaches 360°.

METHODS

Synthetic procedures

Further details regarding the synthetic procedures and characterization can be found in the supplemental information.

Please cite this article in press as: Heard et al., Two $(Ag^{I}_{3}I)_4L_4$ cages elucidate the rules for silver-cluster vertex design, Chem (2025), https://doi.org/10.1016/j.chempr.2025.102456

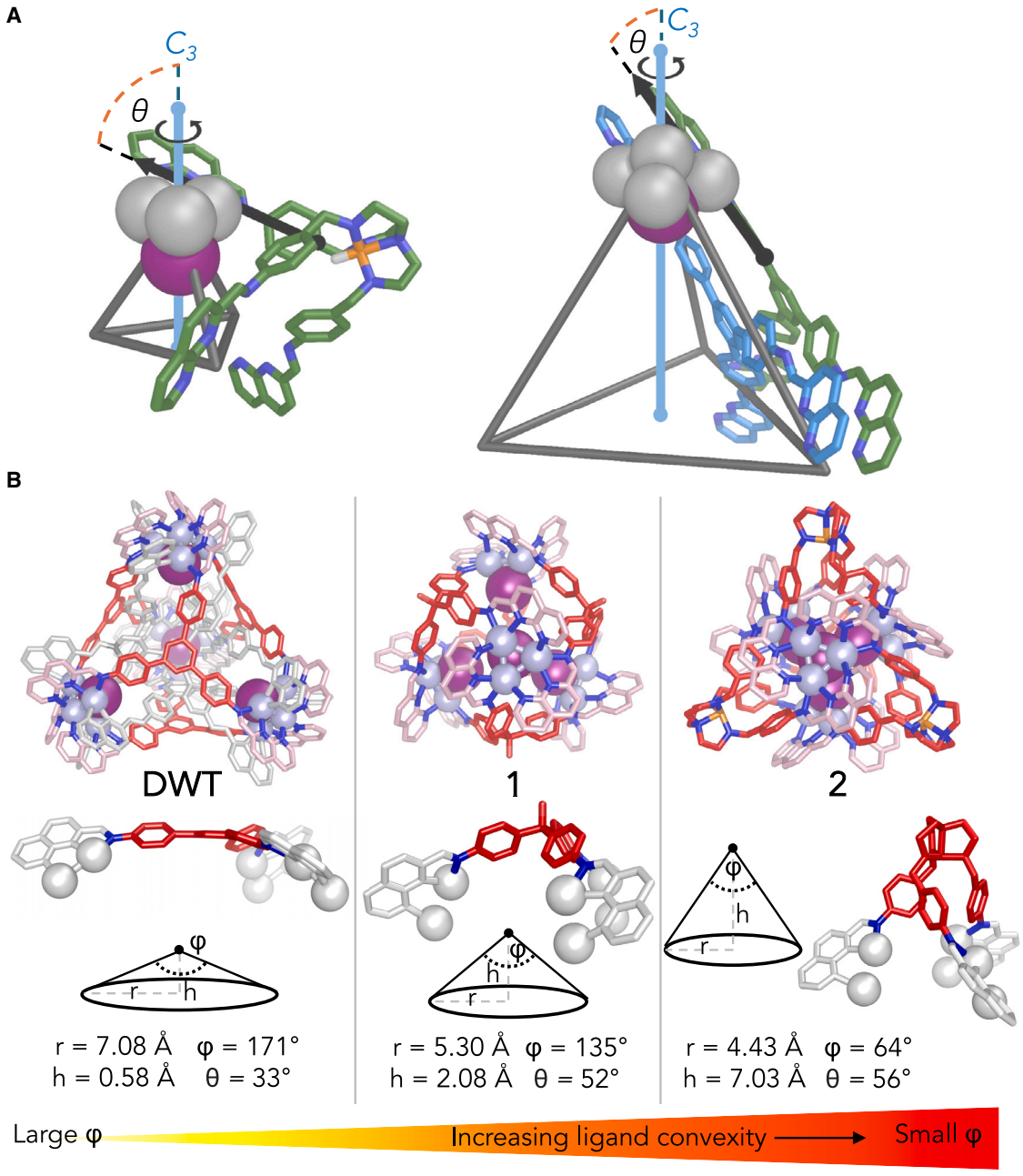

Figure 4. Parameters defining cluster formation

(A) The approach angle, θ: the angle between the chelate plane of the ligand (represented by the black arrows) and the principal symmetry axis (blue line) of the silver cluster vertex.[75]

(B) The convexity, ϕ: the angle at the apex of a cone with a base defined by the three ligand imine nitrogen atoms and an apex at the junction point of the ligand.

Visible and UVRR spectroscopy

Samples were analyzed in powder form and deposited on quartz slides. Raman spectra were acquired on an Invia Renishaw spectrometer (50) using a 785 nm laser (1% laser power, 10 accumulations). Spectra were recorded on different areas of the sample, and average spectra are shown.

UVRR spectra were obtained using the experimental setup available at the BL10.2-IUVS beamline of Elettra Sincrotrone Trieste (Italy). The excitation wavelength at 213 nm was provided by a passively Q-switched laser (FQSS 213-Q, Crylas, 0.9 mW on the sample). The UVRR spectra were recorded on liquid samples (diluted in MeCN) placed in suprasil quartz cuvettes by keeping the temperature fixed at 298 K. The Raman signal was collected in back-scattered geometry and analyzed through a single-pass Czerny-Turner spectrometer (Trivista 557, Princeton Instruments, 750 mm of focal length), equipped with a holographic

Please cite this article in press as: Heard et al., Two $(Ag^{I}_{3}I)_4L_4$ cages elucidate the rules for silver-cluster vertex design, Chem (2025), https://doi.org/10.1016/j.chempr.2025.102456

CellPress
OPEN ACCESS

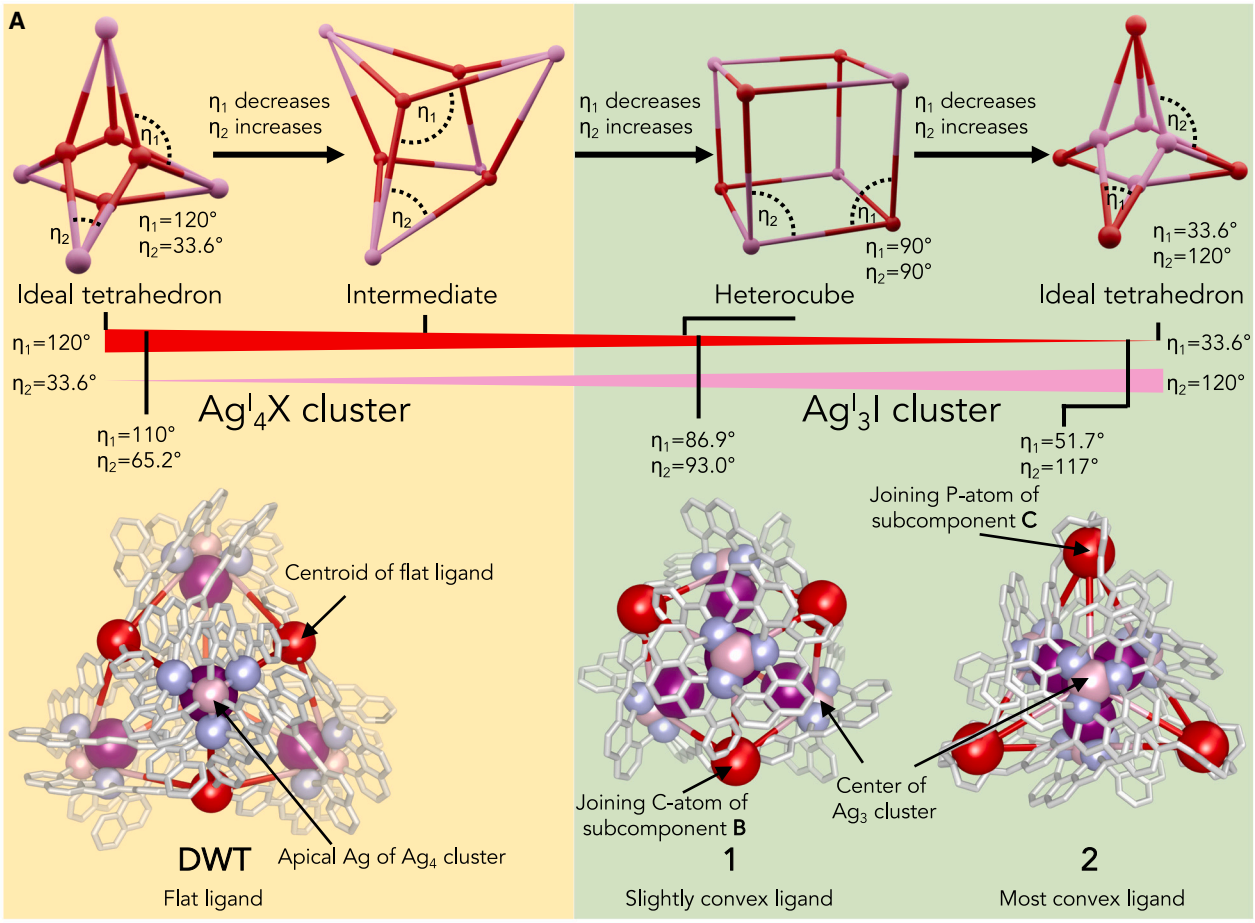

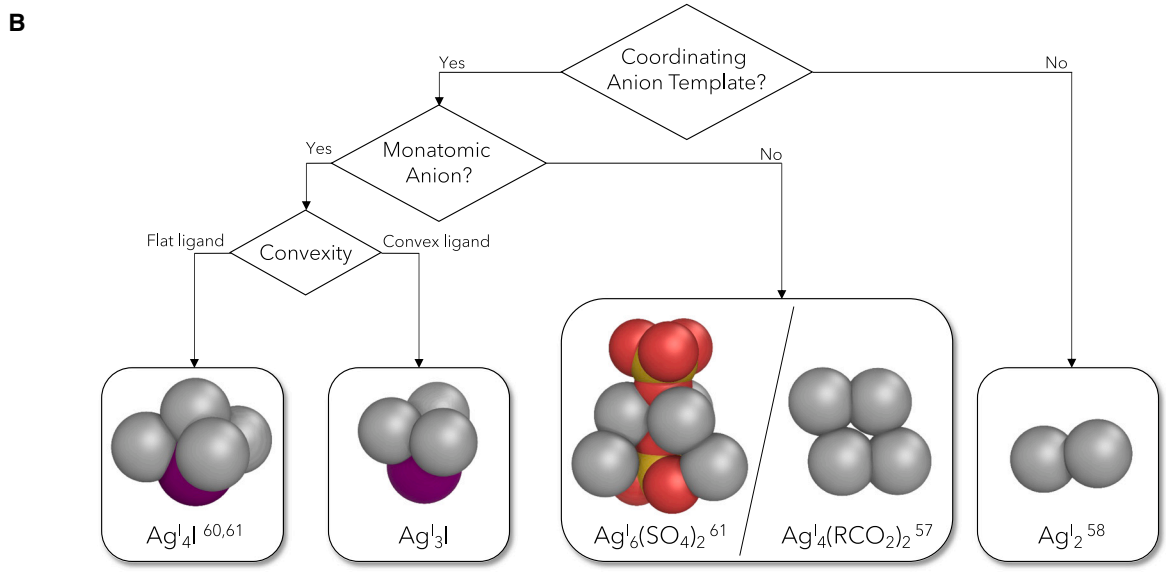

Figure 5. A taxonomy of silver-naphthyridine clusters that form cage vertices

(A) Application of the O'Keeffe and Yaghi analysis[72] for the relationship of angles inside a heterocube to our series of silver cluster tetrahedra, explaining the two distinct silver cluster regimes. The red spheres indicate the junction point of the three arms of a tritopic ligand, and the pink spheres indicate the apical silver(I) of an $Ag^{I}_{4}I$ cluster or the centroid of a flat Ag^{I}_{3} cluster.

(B) Flow chart to determine vertex cluster structure among the known silver-naphthyridine assemblies.

grating at 3,600 g/mm and detected using a UV-enhanced CCD camera. The resolution was set at about 0.9 cm^{-1}/pixel. All the UVRR spectra have been subtracted from the spectral contribution coming from the solvent MeCN, which is practically negligible in the wavenumber range of interest.

RESOURCE AVAILABILITY

Lead contact

Further information and requests for resources should be directed to and will be fulfilled by the lead contact, Jonathan R. Nitschke (jrn34@cam.ac.uk).

Materials availability

Detailed information about the preparation and characterization of new compounds is provided in the supplemental information.

Data and code availability

Crystallographic data for cages PhMe ⊂**1-I**, **2-I**·12PF_6^-, and **2-I**·12BF_4^- can be accessed free-of-charge from the Cambridge Crystallographic Data Centre, accession numbers CCDC: 2306614, CCDC: 2306615, and CCDC: 2306843, respectively.

ACKNOWLEDGMENTS

We thank Diamond Light Source (UK) for synchrotron beamtime on I19 (CY21497). This work was supported by the Defense Advanced Research Projects Agency MIMS program cooperative agreement HR00112420301. The views, opinions, and/or findings expressed are those of the author and should not be interpreted as representing the official views or policies of the Department of Defense or the US Government. This study was supported by the UK Engineering and Physical Sciences Research Council (EPSRC, EP/T031603/1, and EP/P027067/1). A.W.H. is the recipient of an Astex Pharmaceuticals Sustaining Innovation post-doctoral award. S.E.C. is the recipient of a PhD studentship from BP through the BP International Centre for Advanced Materials (bp-ICAM). C.T.M. thanks the Leverhulme Trust, the Isaac Newton Trust, and Sidney Sussex College, Cambridge, for financial support. We acknowledge Elettra Sincrotrone Trieste for providing access to its synchrotron radiation facilities (proposal number 20220534), and we thank M. Tortora for assistance in using beamline IUVS. We thank networking support from COST Action CA17139 (eutopia.unitn.eu), funded by COST (www.cost.eu).

AUTHOR CONTRIBUTIONS

Investigation, A.W.H., S.E.C., C.T.M., T.K.R., P.R., and B.R.; writing—original draft: A.W.H. and S.E.C.; supervision, A.W.H., C.T.M., T.K.R., S.M., and J.R.N.; resources, S.M., B.R., and J.R.N.; writing—review and editing, all authors; conceptualization, S.M. and J.R.N.

DECLARATION OF INTERESTS

The authors declare no competing interests.

SUPPLEMENTAL INFORMATION

Supplemental information can be found online at https://doi.org/10.1016/j.chempr.2025.102456.

Received: October 1, 2024
Revised: November 13, 2024
Accepted: January 28, 2025
Published: March 7, 2025

REFERENCES

1. McConnell, A.J. (2022). Metallosupramolecular cages: from design principles and characterisation techniques to applications. Chem. Soc. Rev. *51*, 2957–2971. https://doi.org/10.1039/d1cs01143j.
2. McTernan, C.T., Davies, J.A., and Nitschke, J.R. (2022). Beyond Platonic: How to Build Metal-Organic Polyhedra Capable of Binding Low-Symmetry, Information-Rich Molecular Cargoes. Chem. Rev. *122*, 10393–10437. https://doi.org/10.1021/acs.chemrev.1c00763.
3. Fujita, D., Ueda, Y., Sato, S., Mizuno, N., Kumasaka, T., and Fujita, M. (2016). Self-assembly of tetravalent Goldberg polyhedra from 144 small components. Nature *540*, 563–566. https://doi.org/10.1038/nature20771.
4. Cullen, W., Misuraca, M.C., Hunter, C.A., Williams, N.H., and Ward, M.D. (2016). Highly efficient catalysis of the Kemp elimination in the cavity of a cubic coordination cage. Nat. Chem. *8*, 231–236. https://doi.org/10.1038/nchem.2452.
5. Davies, J.A., Ronson, T.K., and Nitschke, J.R. (2022). Twisted rectangular subunits self-assemble into a ferritin-like capsule. Chem *8*, 1099–1106. https://doi.org/10.1016/j.chempr.2022.01.003.
6. Ronson, T.K., Wang, Y., Baldridge, K., Siegel, J.S., and Nitschke, J.R. (2020). An S_{10}-Symmetric 5-Fold Interlocked [2]Catenane. J. Am. Chem. Soc. *142*, 10267–10272. https://doi.org/10.1021/jacs.0c03349.
7. Zhu, Z.Z., Tian, C.B., and Sun, Q.F. (2021). Coordination-Assembled Molecular Cages with Metal Cluster Nodes. Chem. Rec. *21*, 498–522. https://doi.org/10.1002/tcr.202000130.
8. Su, K., Wu, M., Yuan, D., and Hong, M. (2018). Interconvertible vanadium-seamed hexameric pyrogallol[4]arene nanocapsules. Nat. Commun. *9*, 4941. https://doi.org/10.1038/s41467-018-07427-z.
9. Liu, G., Ju, Z., Yuan, D., and Hong, M. (2013). In situ construction of a coordination zirconocene tetrahedron. Inorg. Chem. *52*, 13815–13817. https://doi.org/10.1021/ic402428m.
10. Liu, G., Zeller, M., Su, K., Pang, J., Ju, Z., Yuan, D., and Hong, M. (2016). Controlled Orthogonal Self-Assembly of Heterometal-Decorated Coordination Cages. Chemistry *22*, 17345–17350. https://doi.org/10.1002/chem.201604264.
11. Cotton, F.A., Daniels, L.M., Lin, C., Murillo, C.A., and Murillo, C.A. (1999). The designed 'self-assembly' of a three-dimensional molecule containing six quadruply-bonded Mo_2^{4+} units. Chem. Commun. *9*, 841–842. https://doi.org/10.1039/a901645g.
12. Jiang, X.F., Deng, W., Jin, R., Qin, L., and Yu, S.Y. (2014). Self-assembly of tri-pyrazolate linked cages with di-palladium coordination motifs. Dalton Trans. *43*, 16015–16024. https://doi.org/10.1039/c4dt01745e.
13. Jiao, J., Tan, C., Li, Z., Liu, Y., Han, X., and Cui, Y. (2018). Design and Assembly of Chiral Coordination Cages for Asymmetric Sequential Reactions. J. Am. Chem. Soc. *140*, 2251–2259. https://doi.org/10.1021/jacs.7b11679.
14. Howlader, P., and Mukherjee, P.S. (2016). Face and edge directed self-assembly of Pd_{12} tetrahedral nano-cages and their self-sorting. Chem. Sci. *7*, 5893–5899. https://doi.org/10.1039/c6sc02012g.
15. Tan, C., Jiao, J., Li, Z., Liu, Y., Han, X., and Cui, Y. (2018). Design and Assembly of a Chiral Metallosalen-Based Octahedral Coordination Cage for Supramolecular Asymmetric Catalysis. Angew. Chem. Int. Ed. Engl. *57*, 2085–2090. https://doi.org/10.1002/anie.201711310.
16. Lu, W., Yuan, D., Yakovenko, A., and Zhou, H.C. (2011). Surface functionalization of metal-organic polyhedron for homogeneous cyclopropanation catalysis. Chem. Commun. (Camb) *47*, 4968–4970. https://doi.org/10.1039/c1cc00030f.
17. Wu, Y., Xie, M., Jin, J.-K., Zhang, Z.-Y., Hu, H., Tian, Y.-P., Xiao, Y.-Q., Ning, G.-H., Li, D., and Jiang, X. (2022). A Copper Iodide Cluster-Based Metal–Organic Polyhedra for Photocatalytic Click Chemistry. Small Structures *3*, 2100155. https://doi.org/10.1002/sstr.202100155.
18. Augustyniak, A.W., Fandzloch, M., Domingo, M., Łakomska, I., and Navarro, J.A. (2015). A vanadium(IV) pyrazolate metal-organic polyhedron

with permanent porosity and adsorption selectivity. Chem. Commun. (Camb) *51*, 14724–14727. https://doi.org/10.1039/c5cc05913e.

19. Jiang, X.F., Hau, F.K.W., Sun, Q.F., Yu, S.Y., and Yam, V.W.W. (2014). From $\{Au^{I}\cdots Au^{I}\}$-Coupled Cages to the Cage-Built 2-D $\{Au^{I}\cdots Au^{I}\}$ Arrays: $Au^{I}\cdots Au^{I}$ Bonding Interaction Driven Self-Assembly and Their AgI Sensing and Photo-Switchable Behavior. J. Am. Chem. Soc. *136*, 10921–10929. https://doi.org/10.1021/ja502295c.

20. Peng, S.-K., Yang, H., Luo, D., Xie, M., Tang, W.-J., Ning, G.-H., and Li, D. (2022). Enhancing photoluminescence efficiency of atomically precise copper(I) nanoclusters through a solvent-induced structural transformation. Inorg. Chem. Front. *9*, 5327–5334. https://doi.org/10.1039/d2qi01427k.

21. Zhang, Y., Wang, X., Li, S., Song, B., Shao, K., and Su, Z. (2016). Ligand-Directed Assembly of Polyoxovanadate-Based Metal-Organic Polyhedra. Inorg. Chem. *55*, 8770–8775. https://doi.org/10.1021/acs.inorgchem.6b01338.

22. Breen, J.M., Clérac, R., Zhang, L., Cloonan, S.M., Kennedy, E., Feeney, M., McCabe, T., Williams, D.C., and Schmitt, W. (2012). Self-assembly of hybrid organic-inorganic polyoxovanadates: functionalised mixed-valent clusters and molecular cages. Dalton Trans. *41*, 2918–2926. https://doi.org/10.1039/c2dt11153e.

23. Gong, Y., Tao, Y., Xu, N., Sun, C., Wang, X., and Su, Z. (2019). Two polyoxovanadate-based metal-organic polyhedra with undiscovered "near-miss Johnson solid" geometry. Chem. Commun. (Camb) *55*, 10701–10704. https://doi.org/10.1039/c9cc05984a.

24. Li, X.-X., Zhao, D., and Zheng, S.-T. (2019). Recent advances in POM-organic frameworks and POM-organic polyhedra. Coord. Chem. Rev. *397*, 220–240. https://doi.org/10.1016/j.ccr.2019.07.005.

25. Cotton, F.A., Lei, P., Lin, C., Murillo, C.A., Wang, X., Yu, S.Y., and Zhang, Z.X. (2004). A calix[4]arene carceplex with four Rh_2^{4+} fasteners. J. Am. Chem. Soc. *126*, 1518–1525. https://doi.org/10.1021/ja0396899.

26. Li, J.R., and Zhou, H.C. (2010). Bridging-ligand-substitution strategy for the preparation of metal-organic polyhedra. Nat. Chem. *2*, 893–898. https://doi.org/10.1038/nchem.803.

27. El-Sayed, E.M., Yuan, Y.D., Zhao, D., and Yuan, D. (2022). Zirconium Metal-Organic Cages: Synthesis and Applications. Acc. Chem. Res. *55*, 1546–1560. https://doi.org/10.1021/acs.accounts.1c00654.

28. Schmidbaur, H., and Schier, A. (2015). Argentophilic interactions. Angew. Chem. Int. Ed. Engl. *54*, 746–784. https://doi.org/10.1002/anie.201405936.

29. Cuerva, M., García-Fandiño, R., Vázquez-Vázquez, C., López-Quintela, M.A., Montenegro, J., and Granja, J.R. (2015). Self-Assembly of Silver Metal Clusters of Small Atomicity on Cyclic Peptide Nanotubes. ACS Nano *9*, 10834–10843. https://doi.org/10.1021/acsnano.5b03445.

30. Horiuchi, S., Moon, S., Ito, A., Tessarolo, J., Sakuda, E., Arikawa, Y., Clever, G.H., and Umakoshi, K. (2021). Multinuclear Ag Clusters Sandwiched by Pt Complex Units: Fluxional Behavior and Chiral-at-Cluster Photoluminescence. Angew. Chem. Int. Ed. Engl. *60*, 10654–10660. https://doi.org/10.1002/anie.202101460.

31. Sarwa, A., Białońska, A., Garbicz, M., and Szyszko, B. (2023). Plenates: Anion-Dependent Self-Assembly of the Pyrrole Cage Encapsulating Silver(I) Clusters. Chemistry *29*, e202203850.

32. Batsanov, S.S. (2011). Thermodynamic determination of van der Waals radii of metals. J. Mol. Struct. *990*, 63–66. https://doi.org/10.1016/j.molstruc.2010.12.055.

33. Álvarez, S. (2021). Formas y conformaciones de anillos y clústeres inorgánicos de cuatro átomosUn estudio estructural mediante medidas continuas de forma. An. Quim. *117*, 219–225.

34. Kwon, H., Pietrasiak, E., Ohhara, T., Nakao, A., Chae, B., Hwang, C.C., Jung, D., Hwang, I.C., Ko, Y.H., Kim, K., and Lee, E. (2021). Programmable Synthesis of Silver Wheels. Inorg. Chem. *60*, 6403–6409. https://doi.org/10.1021/acs.inorgchem.1c00106.

35. Petit, C., Lixon, P., and Pileni, M.P. (1993). In situ synthesis of silver nanocluster in AOT reverse micelles. J. Phys. Chem. *97*, 12974–12983. https://doi.org/10.1021/j100151a054.

36. Kunwar, P., Hassinen, J., Bautista, G., Ras, R.H.A., and Toivonen, J. (2014). Direct Laser Writing of Photostable Fluorescent Silver Nanoclusters in Polymer Films. ACS Nano *8*, 11165–11171. https://doi.org/10.1021/nn5059503.

37. Kunwar, P., Hassinen, J., Bautista, G., Ras, R.H.A., and Toivonen, J. (2016). Sub-micron scale patterning of fluorescent silver nanoclusters using low-power laser. Sci. Rep. *6*, 23998. https://doi.org/10.1038/srep23998.

38. Yuan, Y.-X., Zhang, J.-N., Wang, J.-R., Li, K., and Zang, S.-Q. (2024). Chiral silver cluster-based light-harvesting systems: Enantioselective chirality transfer and amplified circularly polarized luminescence. Chem *10*, 1766–1782. https://doi.org/10.1016/j.chempr.2024.01.028.

39. Malola, S., and Häkkinen, H. (2024). On transient absorption and dual emission of the atomically precise, DNA-stabilized silver nanocluster $Ag_{16}Cl_2$. Chem. Commun. (Camb) *60*, 3315–3318. https://doi.org/10.1039/d3cc06085c.

40. Shang, L., Dong, S., and Nienhaus, G.U. (2011). Ultra-small fluorescent metal nanoclusters: Synthesis and biological applications. Nano Today *6*, 401–418. https://doi.org/10.1016/j.nantod.2011.06.004.

41. Teramoto, M., Iwata, K., Yamaura, H., Kurashima, K., Miyazawa, K., Kurashige, Y., Yamamoto, K., and Murahashi, T. (2018). Three-Dimensional Sandwich Nanocubes Composed of 13-Atom Palladium Core and Hexakis-Carbocycle Shell. J. Am. Chem. Soc. *140*, 12682–12686. https://doi.org/10.1021/jacs.8b07430.

42. Gu, J., Xu, Y., and Lu, J. (2023). Atom-Precise Low-Nuclearity Cluster Catalysis: Opportunities and Challenges. ACS Catal. *13*, 5609–5634. https://doi.org/10.1021/acscatal.3c01449.

43. Guo, W., Yuan, J., and Wang, E. (2009). Oligonucleotide-stabilized Ag nanoclusters as novel fluorescence probes for the highly selective and sensitive detection of the Hg^{2+} ion. Chem. Commun. (Camb) *23*, 3395–3397. https://doi.org/10.1039/b821518a.

44. Shen, J., Wang, Z., Sun, D., Liu, G., Yuan, S., Kurmoo, M., and Xin, X. (2017). Self-assembly of water-soluble silver nanoclusters: superstructure formation and morphological evolution. Nanoscale *9*, 19191–19200. https://doi.org/10.1039/c7nr06359h.

45. Han, F., Li, J., Wang, W., Wang, M., and Li, L. (2022). Synthesis of silver nanoclusters by irradiation reduction and detection of Cr^{3+} ions. RSC Adv. *12*, 33207–33214. https://doi.org/10.1039/d2ra06536c.

46. Feng, Y., Fu, F., Zeng, L., Zhao, M., Xin, X., Liang, J., Zhou, M., Fang, X., Lv, H., and Yang, G.Y. (2024). Atomically Precise Silver Clusters Stabilized by Lacunary Polyoxometalates with Photocatalytic CO_2 Reduction Activity. Angew. Chem. Int. Ed. Engl. *63*, e202317341. https://doi.org/10.1002/anie.202317341.

47. Yan, L.-L., and Yam, V.W.-W. (2024). Evolution of Polynuclear Gold(I) Sulfido Complexes from Clusters and Cages to Macrocycles. J. Am. Chem. Soc. *146*, 609–616. https://doi.org/10.1021/jacs.3c10381.

48. Hatano, A., Sugawa, T., Mimura, R., Kataoka, S., Yamamoto, K., Omoda, T., Zhu, B., Tian, Y., Sakaki, S., and Murahashi, T. (2023). Isolation and Structures of Polyarene Palladium Nanoclusters. J. Am. Chem. Soc. *145*, 15030–15035. https://doi.org/10.1021/jacs.3c02849.

49. He, X., Gao, C.Y., Wang, M.X., and Zhao, L. (2012). Designed synthesis of a metal cluster-pillared coordination cage. Chem. Commun. (Camb) *48*, 10877–10879. https://doi.org/10.1039/c2cc36250c.

50. Yang, Y., Guo, S., Zhang, Q., Guan, Z.J., and Wang, Q.M. (2024). A Cages-on-Cluster Structure Constructed by Post-Clustering Covalent Modifications and Guest-Enabled Stimuli-Responsive Luminescence. Angew. Chem. Int. Ed. Engl. *63*, e202404798. https://doi.org/10.1002/anie.202404798.

51. Banerjee, R., Chakraborty, D., and Mukherjee, P.S. (2023). Molecular Barrels as Potential Hosts: From Synthesis to Applications. J. Am. Chem. Soc. *145*, 7692–7711. https://doi.org/10.1021/jacs.3c01084.

52. Segarra, C., Guisado-Barrios, G., Hahn, F.E., and Peris, E. (2014). Hexanuclear Cylinder-Shaped Assemblies of Silver and Gold from Benzene–Hexa-*N*-heterocyclic Carbenes. Organometallics *33*, 5077–5080. https://doi.org/10.1021/om500729b.

53. Hahn, F.E., Radloff, C., Pape, T., and Hepp, A. (2008). Synthesis of silver(I) and gold(I) complexes with cyclic tetra- and hexacarbene ligands. Chemistry *14*, 10900–10904. https://doi.org/10.1002/chem.200801877.

54. Tsuda, T., Ohba, S., Takahashi, M., and Ito, M. (1989). Structures of 1,8-naphthyridine silver(I) perchlorate, quinoxaline silver(I) perchlorate and phthalazine silver(I) nitrate. Acta Crystallogr. C Cryst. Struct. Commun. *45*, 887–890. https://doi.org/10.1107/s0108270188014507.

55. Ašanin, D.P., Skaro Bogojevic, S., Perdih, F., Andrejević, T.P., Milivojevic, D., Aleksic, I., Nikodinovic-Runic, J., Glišić, B.Đ., Turel, I., and Djuran, M.I. (2021). Structural Characterization, Antimicrobial Activity and BSA/DNA Binding Affinity of New Silver(I) Complexes with Thianthrene and 1,8-Naphthyridine. Molecules *26*, 1871. https://doi.org/10.3390/molecules26071871.

56. Wang, Y., and Okabe, N. (2005). Tetrakis(μ_2-1,8-naphthyridine)-1:2κ^4N:N';3:4κ4N:N'-bis(μ^2-salicylato)-1:4κ^2O:O';2:3κ^2O:O'-tetrakis(salicylic acid)-1κO,2κO,3κO,4κO-tetrasilver(I)(4 Ag-Ag). Acta Cryst. C *61*, M263–M265. https://doi.org/10.1107/S0108270105010498.

57. Carpenter, J.P., McTernan, C.T., Ronson, T.K., and Nitschke, J.R. (2019). Anion Pairs Template a Trigonal Prism with Disilver Vertices. J. Am. Chem. Soc. *141*, 11409–11413. https://doi.org/10.1021/jacs.9b05432.

58. Carpenter, J.P., Ronson, T.K., Rizzuto, F.J., Héliot, T., Grice, P., and Nitschke, J.R. (2022). Incorporation of a Phosphino(pyridine) Subcomponent Enables the Formation of Cages with Homobimetallic and Heterobimetallic Vertices. J. Am. Chem. Soc. *144*, 8467–8473. https://doi.org/10.1021/jacs.2c02261.

59. Clark, S.E., Heard, A.W., McTernan, C.T., Ronson, T.K., Rossi, B., Rozhin, P., Marchesan, S., and Nitschke, J.R. (2023). A Double-Walled Tetrahedron with Ag^{I}_4 Vertices Binds Different Guests in Distinct Sites. Angew. Chem. Int. Ed. Engl. *62*, e202301612. https://doi.org/10.1002/anie.202301612.

60. McTernan, C.T., Ronson, T.K., and Nitschke, J.R. (2021). Selective Anion Binding Drives the Formation of $Ag^{I}_8L_6$ and $Ag^{I}_{12}L_6$ Six-Stranded Helicates. J. Am. Chem. Soc. *143*, 664–670. https://doi.org/10.1021/jacs.0c11905.

61. Zhang, D., Ronson, T.K., Zou, Y.Q., and Nitschke, J.R. (2021). Metal-organic cages for molecular separations. Nat. Rev. Chem. *5*, 168–182. https://doi.org/10.1038/s41570-020-00246-1.

62. Kaphan, D.M., Levin, M.D., Bergman, R.G., Raymond, K.N., and Toste, F.D. (2015). A supramolecular microenvironment strategy for transition metal catalysis. Science *350*, 1235–1238. https://doi.org/10.1126/science.aad3087.

63. Howlader, P., Das, P., Zangrando, E., and Mukherjee, P.S. (2016). Urea-Functionalized Self-Assembled Molecular Prism for Heterogeneous Catalysis in Water. J. Am. Chem. Soc. *138*, 1668–1676. https://doi.org/10.1021/jacs.5b12237.

64. Fang, S., Sun, W., Lin, C., Huang, F., and Li, H. (2023). Self-Assembled Cage for In Situ Detecting Silver Cation in Water. Inorg. Chem. *62*, 1776–1780. https://doi.org/10.1021/acs.inorgchem.1c03825.

65. Hamacek, J., Borkovec, M., and Piguet, C. (2006). Simple thermodynamics for unravelling sophisticated self-assembly processes. Dalton Trans. *12*, 1473–1490. https://doi.org/10.1039/b518461d.

66. Perreault, D., Drouin, M., Michel, A., and Harvey, P.D. (1993). Relationships between metal-metal force constants and metal-metal separations for disilver and dipalladium systems. Crystal and molecular structures of $Ag_2(dmb)_2X_2$ (X = Cl, Br, I; dmb = 1,8-diisocyano-*p*-menthane) and *cis*-$Pd(CNC(CH_3)_3)_2Cl_2$ complexes. Inorg. Chem. *32*, 1903–1912. https://doi.org/10.1021/ic00062a006.

67. Harvey, P. (1996). Reparameterized Herschbach-Laurie empirical relationships between metal-metal distances and force constants applied to homonuclear bi- and polynuclear complexes (M = Cr, Mo, Rh, Pd, Ag, W, Re, Ir, Pt, Au, Hg). Coord. Chem. Rev. *153*, 175–198. https://doi.org/10.1016/0010-8545(95)01225-7.

68. Herschbach, D.R., and Laurie, V.W. (1961). Anharmonic Potential Constants and Their Dependence upon Bond Length. J. Chem. Phys. *35*, 458–464. https://doi.org/10.1063/1.1731952.

69. Bosnick, K.A. (2000). Raman Analysis of Mass-Selected Metal Clusters (University of Toronto).

70. Maglic, J.B., and Lavendomme, R. (2022). MoloVol: an easy-to-use program for analyzing cavities, volumes and surface areas of chemical structures. J. Appl. Crystallogr. *55*, 1033–1044. https://doi.org/10.1107/S1600576722004988.

71. Zhang, D., Ronson, T.K., Mosquera, J., Martinez, A., Guy, L., and Nitschke, J.R. (2017). Anion Binding in Water Drives Structural Adaptation in an Azaphosphatrane-Functionalized $Fe^{II}_4L_4$ Tetrahedron. J. Am. Chem. Soc. *139*, 6574–6577. https://doi.org/10.1021/jacs.7b02950.

72. Tranchemontagne, D.J., Ni, Z., O'Keeffe, M., and Yaghi, O.M. (2008). Reticular chemistry of metal-organic polyhedra. Angew. Chem. Int. Ed. Engl. *47*, 5136–5147. https://doi.org/10.1002/anie.200705008.

73. Groom, C.R., Bruno, I.J., Lightfoot, M.P., and Ward, S.C. (2016). The Cambridge Structural Database. Acta Crystallogr. B Struct. Sci. Cryst. Eng. Mater. *72*, 171–179. https://doi.org/10.1107/S2052520616003954.

74. Shields, D.J., Elkoush, T., Miura-Stempel, E., Mak, C.L., Niu, G.H., Gudmundsdottir, A.D., and Campbell, M.G. (2020). Visible Light Absorption and Long-Lived Excited States in Dinuclear Silver(I) Complexes with Redox-Active Ligands. Inorg. Chem. *59*, 18338–18344. https://doi.org/10.1021/acs.inorgchem.0c02938.

75. Caulder, D.L., and Raymond, K.N. (1999). Supermolecules by Design. Acc. Chem. Res. *32*, 975–982. https://doi.org/10.1021/ar970224v.

76. Wu, K., Ronson, T.K., Su, P., Chen, Z., Goh, L., Heard, A.W., Li, X., Klautzsch, F., Schalley, C.A., Vinković, M., and Nitschke, J.R. (2023). Systematic construction of progressively larger capsules from a fivefold linking pyrrole-based subcomponent. Nat. Synth. *2*, 789–797.